



Iron (II and III) Oxides/Reduced Graphene Oxide/Polypyrrole Ternary Nanocomposite as Electrochemical Supercapacitor Electrode

R. Ghanbari,^{1,2} M. Entezar Shabestari,³ E. Naderi Kalali,² Y. Hu,^{2,z} and S. R. Ghorbani^{1,z}

¹Energy and Advanced Materials Lab, Department of Physics, Faculty of Science, Ferdowsi University of Mashhad, Mashhad, Iran

²State Key Laboratory of Fire Science, University of Science and Technology of China, Hefei, Anhui, 230026, People's Republic of China

³Department of Materials Science and Engineering and Chemical Engineering, Carlos III University of Madrid, Leganes, 28911 Madrid, Spain

In this work, ternary nanocomposites of iron (II and III) oxides/reduced graphene oxide/polypyrrole (iron oxide/rGO/PPy) have been prepared as the electrode materials of the supercapacitor. These nanocomposites were prepared via a facile two-step process including, the synthesis of iron oxides/rGO binary nanohybrids by a one-pot chemical-microwave method and in situ oxidative polymerization. The morphological and structural characterizations of these nanocomposites were demonstrated decoration of the iron oxides on GO sheets and proper formation of iron oxide/rGO/PPy ternary nanocomposites. The electrochemical performance evaluation of the samples revealed charge storage mechanisms in both the binary and ternary nanocomposites. A high specific capacitance of 626.8 F g⁻¹ was obtained for the Fe₂O₃/rGO/PPy nanocomposite at a constant current density of 1 A g⁻¹ in a 1 M H₂SO₄ solution electrolyte. This high specific capacitance (vs 158.2 F g⁻¹ for Fe₃O₄/rGO/PPy) can be assigned to the attendance of both electrical double-layer capacitance (EDLC) and pseudocapacitance mechanisms in its charge storage. The Fe₂O₃/rGO/PPy nanocomposite revealed the highest energy density of 87.05 Wh kg⁻¹ with a corresponding power density of 500 W kg⁻¹. The frequency dependence and relaxation time constant investigation of these ternary nanocomposites revealed an ideal capacitive behavior at very low frequency and resistive behavior at the higher frequencies.

© 2021 The Electrochemical Society ("ECS"). Published on behalf of ECS by IOP Publishing Limited. [DOI: 10.1149/1945-7111/abef60]

Manuscript submitted December 31, 2020; revised manuscript received February 15, 2021. Published March 30, 2021.

Supplementary material for this article is available [online](#)

In recent years environmentally friendly energy storage devices such as full cells, rechargeable batteries, and supercapacitors have developed.¹⁻⁴ Among them, supercapacitors have become of great interest due to their superior properties, such as rapid charge/discharge process, high power density, and long cycle life.^{2,5,6} Supercapacitors in terms of charge storage mechanisms are classified to (i) EDLCs where electrolyte ions are adsorbed onto the surface of an electrode, and (ii) pseudocapacitors where the charges are stored by fast and reversible faradaic reactions.^{2,7}

Typically, the electrode materials of supercapacitors can be classified into: carbonaceous materials,^{6,8} transition metals (metal nitrates, oxyhydroxides, sulfides or oxides),⁹⁻¹¹ and conducting polymers.^{12,13} Among of carbon-based materials, graphene, with a 2-dimensional structure of carbon atoms with an sp²-hybridized, has a high theoretical specific surface area and excellent electrical properties.¹⁴ It exhibits a good EDLC, but the agglomeration and weak mechanical stability of graphene sheets limit the energy density and cycling stability of supercapacitors.¹⁵ The transition metal oxides are a proper candidate to improve the energy density of graphene-based supercapacitors. Some transition metal oxides (such as WO₃, MoO₃, Nb₂O₅, RuO₂, NiO, Fe₂O₃, CoO, Co₃O₄, MnO₂, and V₂O₅) display excellent pseudocapacitance behavior and that can avoid re-agglomeration of graphene sheets in their composite with graphene oxide (GO).¹⁶ These metal oxides mostly have high theoretical capacitance, while suffer from poor electrical conductivity and low cycling stability.¹⁶ To solve the low-conductivity problem of these materials, conducting polymers (such as polypyrrole, polyaniline, and poly(3,4-ethylene dioxythiophene)) are an ideal candidate. Moreover, conductive polymers have the advantage of rapid faradaic reactions and high theoretical capacitance.⁷ However, poor cycling stability of the conductive polymers is their main drawback.¹⁷ To overcome this problem, some ternary graphene-based composite electrodes have been recently proposed.^{11,17-20} For example, the flexible PPy/GO/ZnO

nanocomposite as supercapacitor electrodes showed a specific capacitance of 94.6 F g⁻¹ at 1 A g⁻¹.⁷ Also, the specific capacitance for one-step synthesis of graphene oxide/PPy/silver ternary nanocomposite was reported 370.6 F g⁻¹.²¹ A maximum specific capacitance of 404 F g⁻¹ was reported for a hierarchical MnO₂/PPy/reduced graphene oxide (rGO) hybrid composite electrode, attributing to the strong synergistic effects of their components.¹⁵ Furthermore, Graphene/SnO₂/Polypyrrole nanocomposite was prepared as a supercapacitor electrode material, and its specific capacitance reached 616 F g⁻¹ at a sweep rate of 1 mV s⁻¹.²²

Among the transition metal oxides, iron oxides, due to their high theoretical capacitance, facile synthesis, non-toxic, and eco-friendliness are widely used for energy storage applications.^{20,23} Zhu et al. decorated Fe₂O₃ on rGO platelets as an anode material for Lithium-ion batteries.²³ Magnetite (Fe₃O₄) was synthesized and decorated on graphene sheets using ammonium peroxydisulfate as an initiator and microwave irradiation by Vadahanambi et al.²⁴ Also, Moysiewicz et al. reported a two-step synthesis of PPy/Fe₂O₃/rGO composite as an electrode material for supercapacitor. This electrode material exhibited a specific capacitance of 140 F g⁻¹ and capacitance retention of 93% after 5000 cycles at a current density of 1 A g⁻¹, respectively.¹⁷

In the present work, the iron oxides in the configuration of iron oxides/rGO binary nanohybrid and iron oxides/rGO/PPy ternary nanocomposite have been prepared as the supercapacitor electrode materials. Fe₂O₃/rGO and Fe₃O₄/rGO binary nanohybrids are synthesized by a one-pot chemical-microwave method. In the next step, iron oxide/rGO/PPy ternary nanocomposites are prepared using in situ polymerization of pyrrole onto the iron oxides/rGO. The TEM images, FTIR, and Raman spectroscopy, XRD patterns, and XPS show the proper formation of iron oxide/rGO/PPy ternary nanocomposites. The maximum specific capacitance at a current density of 1 A g⁻¹ has been obtained 626.8 and 158.2 F g⁻¹ for Fe₂O₃/rGO/PPy and Fe₃O₄/rGO/PPy ternary nanocomposite, respectively. The frequency dependence and relaxation time evaluation by electrochemical impedance spectroscopy (EIS) reveals these ternary

^zE-mail: sh.ghorbani@um.ac.ir; yuanhu@ustc.edu.cn

nanocomposites exhibit an ideal capacitive behavior only at very low frequency.

Experiment

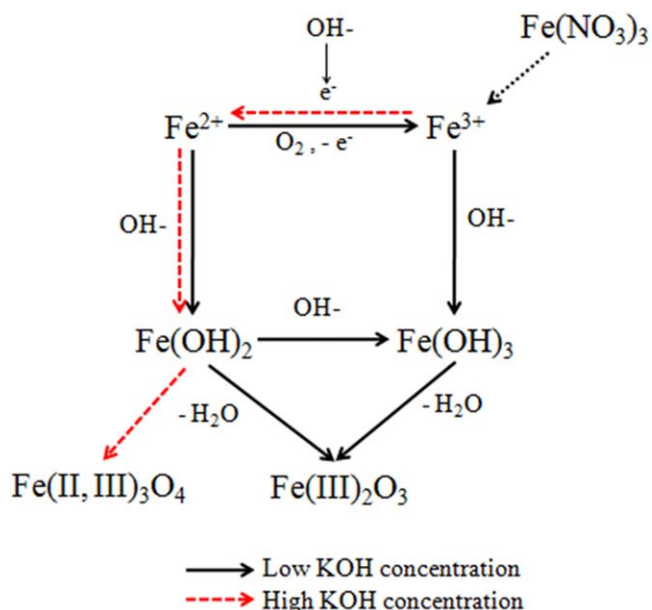
All the used chemical materials in this study were bought from Sinopharm Chemical Reagent Co. Ltd. (Shanghai, China).

Preparation of iron oxide (II and III)/rGO nanohybrids.—GO was synthesized by a modified Hummers and Offeman's method²⁵ as described in Supporting Information. The iron oxide/rGO nanohybrids were prepared by the in situ chemical-microwave method. Briefly, 0.1 g of synthesized GO was dispersed into ethylene glycol by ultrasonication for 30 min (SCENTZ-IID Ultrasonic Homogenizer). Then, 1.16 g of iron (III) nitrate nonahydrate dissolved in 200 ml of ethylene glycol was added into the GO suspension and ultrasonicated for 1 min at 500 W. The iron oxides were synthesized by the different KOH concentration conditions. Based on this, KOH 0.04 M (for Fe₂O₃ and 2 M for Fe₃O₄) solution was added into the mixture drop by drop (for Fe₂O₃ and fast for Fe₃O₄) until its pH reached to 11. A schematic illustration of synthesis of Fe₂O₃ and Fe₃O₄ under the low and high KOH concentration has been shown in Scheme 1. After that, the homogeneous mixture was irradiated by the microwave oven (Midea, M1-L213B21L, china) at 700 W power. After that, the suspension was separated and washed by deionized (DI) water and ethanol. At last, the product was dried by a vacuum oven at 80 °C for 6 h. Thus, the Fe₂O₃/rGO and Fe₃O₄/rGO binary nanohybrids were prepared. The adjusted mass ratio of iron oxides and rGO in the iron oxide/rGO nanohybrids was 2:1.

Preparation of iron (II and III) oxide/rGO/PPy ternary nanocomposite.—The iron oxide/rGO/PPy nanocomposites were further prepared via in situ oxidative polymerization of pyrrole onto the dispersed iron oxide/rGO nanohybrids. The weight ratio of pyrrole to iron oxide/rGO nanohybrid was selected as 10:1. It was found²⁶ that this ratio show the maximum conductivity. Scheme 2 illustrates the synthesis process of iron oxide/rGO/PPy nanocomposite. Briefly, 0.1 g of iron oxide/rGO nanohybrid was dispersed in ethanol, and the freshly distilled pyrrole monomer added into it. The mixture was stirred and cooled in an ice bath under a nitrogen atmosphere. Then, 2.4 g of iron (III) chloride hexahydrate (≥99%) was dissolved in 0.1 M hydrochloric acid, and the product solution was slowly injected into the suspension with stirring. The reaction mixture was allowed to proceed at 0°C–5°C for 24 h. Finally, the solid materials were separated and washed subsequently with DI water and ethanol several times, and dried overnight under a vacuum at 60 °C. The sample of Fe₂O₃/rGO@Fe₃O₄/rGO/PPy hybrid nanocomposite was synthesized in the same way, in which the ratio of Fe₂O₃/rGO to Fe₃O₄/rGO was 1:1 in iron oxide/rGO. The pure PPy was also prepared by using an identical method. All as-prepared ternary nanocomposites were kept in a cool place for followed characterization.

Measurements and characterization.—The morphological and structural characterizations of the samples were studied by the transmission electron microscopy (TEM), Fourier transform infrared (FTIR) and Raman spectroscopy, X-ray powder diffraction (XRD) and X-ray photoelectron spectroscopy (XPS) at room temperature. Specifications of these devices are given in the Supporting Information.

The electrochemical properties of the synthesized materials were measured using a CHI660E Electrochemical Workstation system (Shanghai, China) at ambient temperature. In this system, the counter and reference electrodes were a platinum foil and Ag/AgCl, respectively. For the working electrodes, the mixture was prepared by 80 wt% of the activated material (synthesized materials), 10 wt% of polyvinylidene fluoride, and 10 wt% of activated carbon, which was dispersed in 1-methyl-2-pyrrolidinone. The



Scheme 1. Synthesize of iron (II and III) oxides under the low and high KOH concentration.

obtained slurry was cast onto the glassy carbon electrode by micropipette, and dried at 60 °C for 24 h. The diameter of glassy carbon and the mass loading of the active materials was 3 mm and 0.222 mg, respectively. A 1 M H₂SO₄ solution was used as the electrolyte. Cyclic voltammetry (CV) was done at the different voltage scan rates in the potential window of –0.2 to +0.8 V (vs Ag/AgCl). In the CV plot, the specific capacitance (C_s , F g⁻¹) is given by^{19,27}:

$$C_s = \frac{\int I(V) dV}{m (\Delta V) \vartheta} \quad [1]$$

where I is the current response and the integral part gives the area under the CV plot. ΔV , m and ϑ are the potential window, the mass of active electrode material, and the voltage scan rate, respectively. Also, galvanostatic charge/discharge (GCD) measurements were performed at the different applied current in the potential range of –0.2 to +0.8 V. The specific capacitance is calculated by the following expression from the GCD curves^{19,27}:

$$C_s^{dis} = \frac{I}{m \frac{\Delta V}{\Delta t}} \quad [2]$$

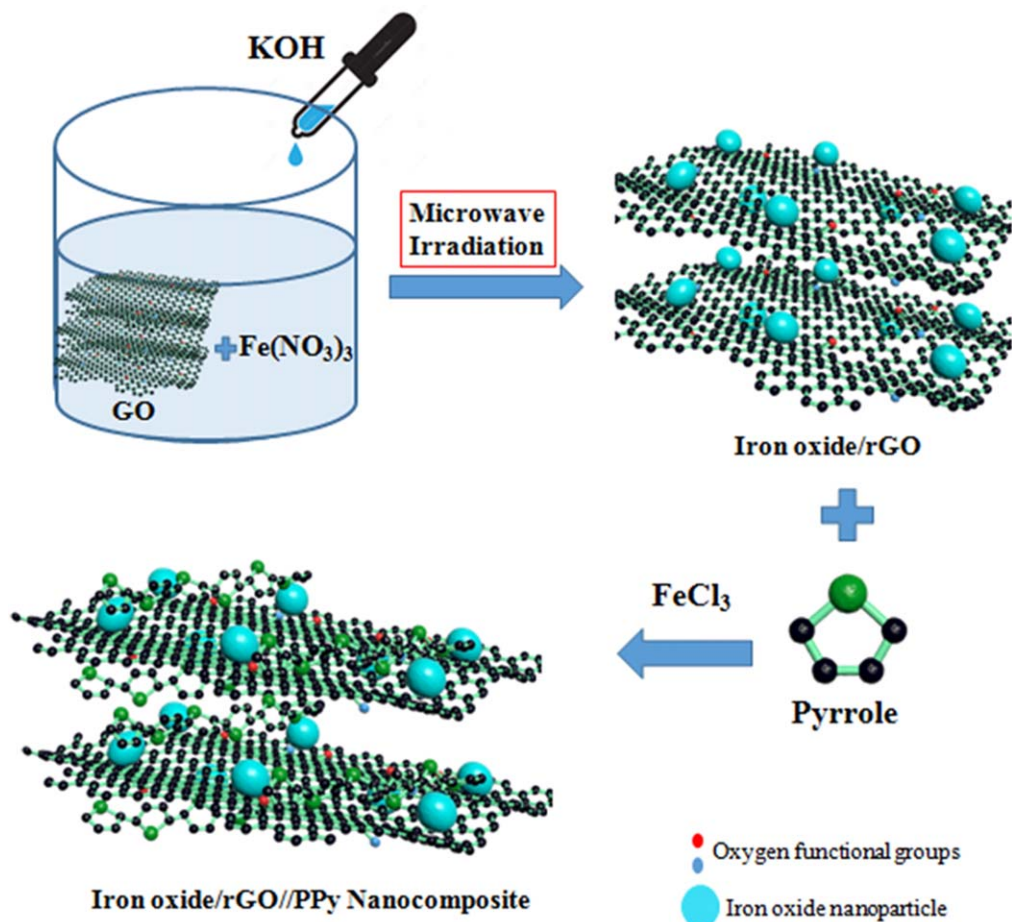
where Δt is the discharge time. EIS measurements were done at an open circuit potential of 0.4 V in the frequency range from 10⁻² to 10⁵ Hz.

Results and Discussion

Microwave irradiation of GO/ethylene glycol solution in the attendance of iron oxide nanoparticles leads to a reduction of GO and direct decoration of iron oxides onto the GO nanosheets simultaneously. This method was resulted in iron oxide/rGO binary nanohybrids.

In Fig. 1, the TEM images of iron oxides/rGO illustrate successful decoration of the iron oxide nanoparticles on the rGO nanosheets and their good exfoliation under microwave irradiation. As can be seen, the Fe₃O₄ decorated nanoparticles are significantly smaller than Fe₂O₃ decorated nanoparticles on rGO nanosheets.

XRD patterns of GO, rGO, and Fe₂O₃/rGO and Fe₃O₄/rGO binary nanohybrid have been presented in Fig. 2a. As can be seen in



Scheme 2. A scheme illustrating the synthesis of iron oxide/rGO/PPy nanocomposite.

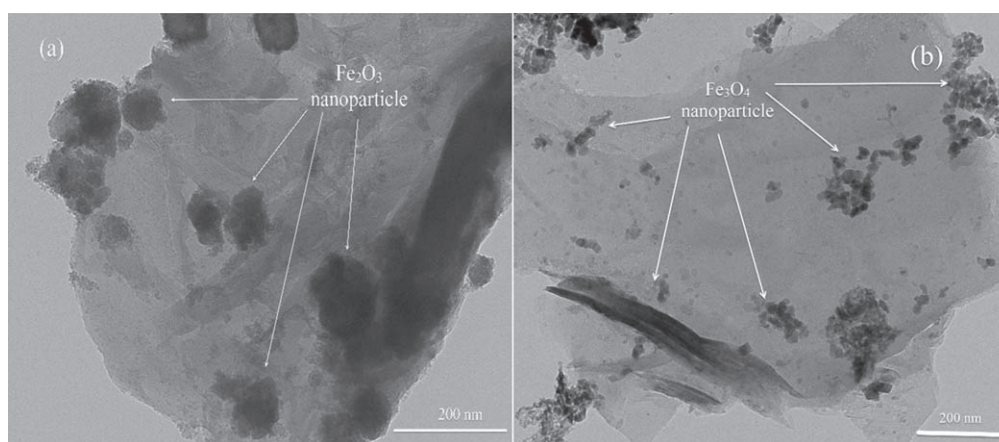


Figure 1. The TEM image of (a) Fe₂O₃/rGO nanohybrid and (b) Fe₃O₄/rGO nanohybrid.

Fig. 2a, the prominent peaks at $2\theta = 24.1, 33.2, 35.8, 41.0, 49.6, 54.1, 62.5, \text{ and } 64.2^\circ$ corresponding to (012), (104), (110), (113), (024), (116), (214), and (300) planes of Fe₂O₃, respectively,¹⁷ confirm the formation of Fe₂O₃ nanoparticles. Also, the diffraction peaks at $30.4, 35.7, 43.4, 54.0, 57.3, 63.0^\circ, \text{ and } 74.6^\circ$ assigning to the (220), (311), (400), (422), (511), (440), and (620) planes of Fe₃O₄, respectively,^{28,29} display the presence of Fe₃O₄ nanoparticles in its binary nanohybrid. The broad diffraction peak at around 26.3° attributing to (002) planes in the rGO implies reducing GO under microwave irradiation in both binary nanohybrids.

In addition, XPS was performed to distinguish between two Fe₂O₃/rGO and Fe₃O₄/rGO binary nanohybrids. The XPS spectra of these binary nanohybrids were shown in Fig. 2b. Results clearly show the presence of C 1s, O 1s, and Fe 2p orbitals at binding energies of 285, 532, and 711 eV, respectively, in these nanocomposites. Figure 2c shows the high-resolution deconvolution of Fe 2p core-level spectra for both the binary nanohybrids. The XPS spectrum of Fe₂O₃/rGO exhibits the Fe 2p_{3/2} and Fe 2p_{1/2} along with a satellite peak at binding energies of 712, 725.8, and 719.6 eV, respectively. The extracted peaks from Fe 2p_{3/2} core orbital at the binding energies of 711.9, 713.4 and 715.0 eV can be assigned to

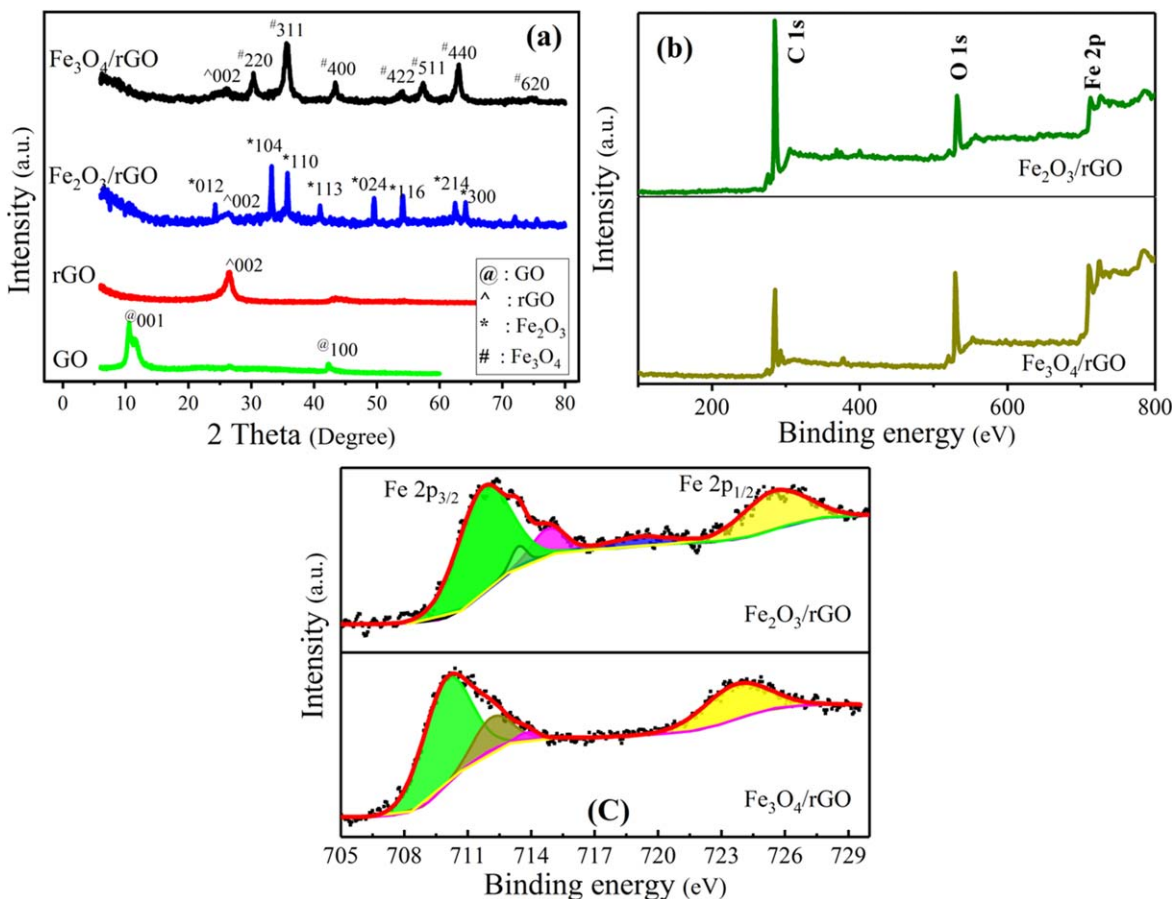


Figure 2. (a) XRD patterns of GO, rGO, Fe₂O₃/rGO nanohybrid, and Fe₃O₄/rGO nanohybrid; (b) XPS spectra and (c) the deconvolution of Fe 2p core-level spectra for Fe₂O₃/rGO and Fe₃O₄/rGO binary nanohybrids.

Fe–Fe, Fe–C and Fe–O bonds, respectively. Also, the Fe 2p_{1/2} peak can correspond to Fe₂–C bonds.³⁰ Similarly, the spectrum of Fe₃O₄/rGO shows the Fe 2p_{3/2} and Fe 2p_{1/2} core orbital at binding energies of 710.3 and 724.2 eV, respectively. The presence of a satellite peak in the spectrum of Fe₂O₃/rGO reveals the oxidation state of +III for Fe that confirms the formation of Fe₂O₃ in this binary nanohybrid. While the spectrum of Fe₃O₄/rGO, which does not display the charge transfer satellite, suggests the mixed oxidation state of +II and +III for Fe and formation of Fe₃O₄ in Fe₃O₄/rGO nanohybrid.^{24,31} Also, the presence of Fe–C and Fe₂–C bonds confirms the decoration of iron oxides on the graphene oxide nanosheets.³⁰ The XPS results reveal that the Fe₂O₃ and Fe₃O₄ nanoparticles have been decorated on the rGO nanosheets during the chemical and microwave irradiation process.

FTIR spectra of rGO, Fe₃O₄/rGO binary nanohybrid, PPy, and Fe₃O₄/rGO/PPy ternary nanocomposite have been shown in Fig. 3a. The located bands at 3436, 1580, and 1118 cm⁻¹ in the rGO spectrum are corresponded to stretching vibrations of –OH, C=C and C–O–C functional groups, respectively.^{20,32} The absorption peaks at 430 and 557 cm⁻¹ in the FTIR spectrum of Fe₃O₄/rGO are attributed to Fe–O group vibration.³³ The attributed peak to C=C vibration is red-shifted to 1569 cm⁻¹ in the spectrum of Fe₃O₄/rGO nanohybrid. In the spectrum of pristine PPy, the peak at 3425 cm⁻¹ is related to the N–H stretching. The absorption band at 1532 cm⁻¹ is assigned to the asymmetric pyrrole ring-stretching vibration.³⁴ This peak has a higher intensity in the spectrum of Fe₃O₄/rGO/PPy nanocomposite due to overlapping with a broad peak of 1569 cm⁻¹ in the Fe₃O₄/rGO spectrum. The absorption bands at 1288 and 1033 cm⁻¹ in the spectrum of PPy indicate in-plane vibration of =C–H and residue oxide groups such as –C–O, respectively,³⁵ which are also observed in the spectrum of Fe₃O₄/rGO/PPy

nanocomposite. Also, the peak at 1160 cm⁻¹ in the spectrum of pure PPy corresponding to stretching vibration of –C–N,¹¹ is blue-shifted to the wavenumber of 1165 cm⁻¹ for Fe₃O₄/rGO/PPy nanocomposite. It may be attributed to the interaction of the nitrogenous groups in PPy with the graphene oxide.²⁰ The absorption band at 855 cm⁻¹ in the FTIR spectrum of Fe₃O₄/rGO is also observed in the spectrum of Fe₃O₄/rGO/PPy nanocomposite. The FTIR spectra of Fe₂O₃/rGO binary nanohybrid and Fe₂O₃/rGO/PPy ternary nanocomposite, shown in Fig. S1 (Supporting Information (available online at stacks.iop.org/JES/168/030543/mmedia)) also, display all these peaks. Therefore, the FTIR spectra confirm the formation of iron oxide/rGO/PPy nanocomposites.

Raman spectra of the samples have been shown in Fig. 3b. Two characteristic D- and G-bands are observed at the wavenumber of 1335 and 1592 cm⁻¹, respectively, for iron oxide/rGO nanohybrids. The peaks at 660 cm⁻¹ (in Fe₂O₃/rGO) and 686 cm⁻¹ (in Fe₃O₄/rGO) confirm the formation of iron oxides/rGO.³⁰ The characteristic peaks of PPy at 938 and 1042 cm⁻¹ correspond to the pyrrole ring deformation and C–H in-plane deformation vibration, respectively.¹¹ As can be seen in Fig. 3b, the D-band in the iron oxide/rGO/PPy nanocomposites shifts to 1567 cm⁻¹, which can be attributed to the π - π interaction of PPy chains with the iron oxide/rGO nanohybrids, suggesting the formation of iron oxide/rGO/PPy nanocomposites.³⁶ The G-band is attributed to E_{2g} mode from the in-plane vibration of sp² carbon, while D-band corresponds to A_{1g} phonons of sp³ carbon atoms in disordered graphite.³⁷ Thus, the ratio of D-band to G-band intensity (I_D/I_G) can be related to the density of defects and the graphitization degree of carbonaceous materials.^{34,38} This ratio was 1.443 and 1.166 for the Fe₂O₃/rGO and Fe₃O₄/rGO, respectively, indicating a decrement in the sizes of in-plane sp² domains and the higher defects of Fe₂O₃/rGO (in comparison with

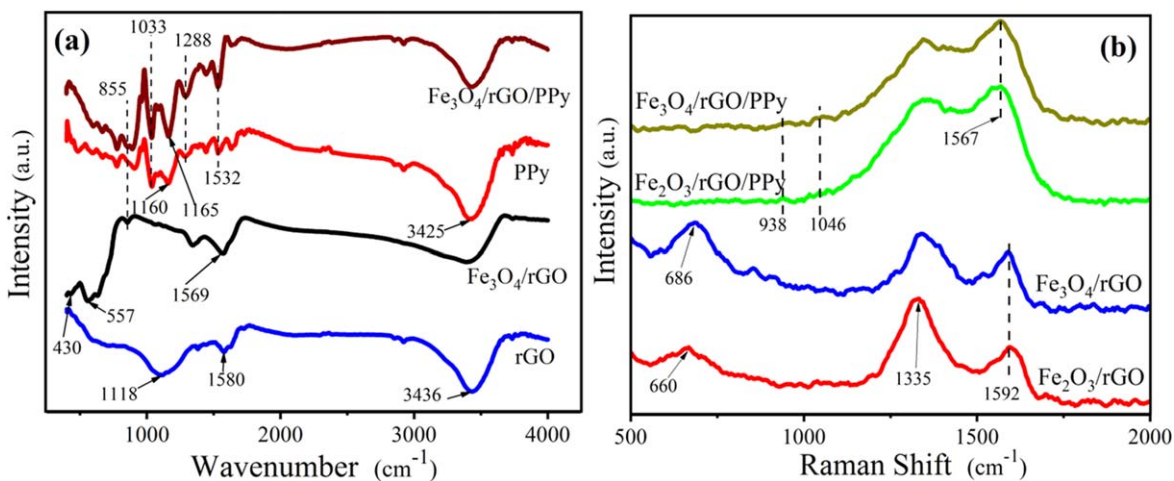


Figure 3. (a) FTIR and (b) Raman spectra of the samples.

$\text{Fe}_3\text{O}_4/\text{rGO}$ nanohybrid. It can be due to a longer reaction time of KOH with a solution of GO in $\text{Fe}_2\text{O}_3/\text{rGO}$ nanohybrid. The I_D/I_G ratio of $\text{Fe}_2\text{O}_3/\text{rGO}/\text{PPy}$ and $\text{Fe}_3\text{O}_4/\text{rGO}/\text{PPy}$ nanocomposite was 0.931 and 0.891, respectively. Decreased the I_D/I_G ratio of ternary nanocomposites (iron oxides/rGO/PPy) compared to binary nanohybrid (iron oxides/rGO) could be related to a decrement in the sizes of sp^2 domains and increasing disorders. That is due to interaction of polypyrrole chains with graphene sheets.

The cyclic voltammetry analyses were done for all the samples at scan rates of 5, 10, 20, 50, and 100 mV s^{-1} . The CV plots of $\text{Fe}_2\text{O}_3/\text{rGO}$ and $\text{Fe}_3\text{O}_4/\text{rGO}$ binary nanohybrid, $\text{Fe}_2\text{O}_3/\text{rGO}/\text{PPy}$, and $\text{Fe}_3\text{O}_4/\text{rGO}/\text{PPy}$ ternary nanocomposite, and $\text{Fe}_2\text{O}_3/\text{rGO}@/\text{Fe}_3\text{O}_4/\text{rGO} / \text{PPy}$ hybrid nanocomposite have been demonstrated in Fig. 4a and b at scan rates of 5 and 100 mV s^{-1} , respectively. The other CV plots have been shown in Figs. S2–S6 in the SI. The presence of peaks and non-rectangular shaped in the CV plots of $\text{Fe}_2\text{O}_3/\text{rGO}$ (in inset Fig. 4a) and $\text{Fe}_3\text{O}_4/\text{rGO}$ binary nanohybrids reveal pseudocapacitance behavior, which can be ascribed to iron oxides redox reactions.⁵ These peaks in the positive and negative current area can be attributed to anodic oxidation and cathodic reduction, respectively.¹⁹ As shown in Fig. 4a, the significant increase of current density in iron oxides/rGO/PPy ternary nanocomposites indicates a notable increment in their specific capacitance. Also, the redox peaks of $\text{Fe}_2\text{O}_3/\text{rGO}$ are observed in the CV plot of $\text{Fe}_2\text{O}_3/\text{rGO}/\text{PPy}$ ternary nanocomposite. However, the redox peaks of $\text{Fe}_3\text{O}_4/\text{rGO}$ have been approximately faded in its ternary nanocomposite. These redox peaks also are observed in the CV plot of $\text{Fe}_2\text{O}_3/\text{rGO}@/\text{Fe}_3\text{O}_4/\text{rGO} / \text{PPy}$ hybrid nanocomposite with a small shift at the potential. Figure 4b illustrates the CV plots of all the samples at a scan rate of 100 mV s^{-1} . It reveals that the redox peaks have become broad and shifted to the higher potential by increasing the scan rate. In Figs. 4a and 4b, it can be seen that the closed-loop area of iron oxides/rGO/PPy ternary nanocomposites has dramatically increased than their binary nanohybrids (iron oxides/rGO) at the same scan rate. The specific capacitance values of the samples were calculated by using Eq. 1 at different scan rates, and the results have been shown in Fig. 4c. The specific capacitance value of 478.2 and 170.5 F g^{-1} was obtained for $\text{Fe}_2\text{O}_3/\text{rGO}/\text{PPy}$ and $\text{Fe}_3\text{O}_4/\text{rGO}/\text{PPy}$ ternary nanocomposite, respectively, at a scan rate of 5 mV s^{-1} . The obtained specific capacitance value of $\text{Fe}_2\text{O}_3/\text{rGO}$ and $\text{Fe}_3\text{O}_4/\text{rGO}$ binary nanohybrid was only 4.4 and 38.7 F g^{-1} , respectively. Therefore, the specific capacitance of $\text{Fe}_2\text{O}_3/\text{rGO}/\text{PPy}$ and $\text{Fe}_3\text{O}_4/\text{rGO}/\text{PPy}$ ternary nanocomposite is about 109 and 4 times larger than that for $\text{Fe}_2\text{O}_3/\text{rGO}$ and $\text{Fe}_3\text{O}_4/\text{rGO}$ binary nanohybrid, respectively, which can be assigned to the efficient combination and the synergistic effect between the components in these both ternary nanocomposites. The specific capacitance value of 225.2 F g^{-1} was

obtained for $\text{Fe}_2\text{O}_3/\text{rGO}@/\text{Fe}_3\text{O}_4/\text{rGO} / \text{PPy}$ hybrid nanocomposite at 5 mV s^{-1} . This value is about 100 F g^{-1} smaller than the calculated specific capacitance (according to the ratio of 1:1 for $\text{Fe}_2\text{O}_3/\text{rGO}$ and $\text{Fe}_3\text{O}_4/\text{rGO}$ in this hybrid nanocomposite: $(C_{\text{Fe}_2\text{O}_3/\text{ternary}} + C_{\text{Fe}_3\text{O}_4/\text{ternary}})/2 = 324.35 \text{ F g}^{-1}$). As it can be seen in Fig. 4c, the specific capacitance decreased to 3.77, 16.79, 177.61, 108.40, and 136.94 F g^{-1} at a scan rate of 100 mV s^{-1} for $\text{Fe}_2\text{O}_3/\text{rGO}$, $\text{Fe}_3\text{O}_4/\text{rGO}$, $\text{Fe}_2\text{O}_3/\text{rGO}/\text{PPy}$, $\text{Fe}_3\text{O}_4/\text{rGO}/\text{PPy}$, and $\text{Fe}_2\text{O}_3/\text{rGO}@/\text{Fe}_3\text{O}_4/\text{rGO} / \text{PPy}$ nanocomposite, respectively. It can be attributed to the inability of ions to the whole diffusion into the internal sites of electrode material that results in to decrease of redox reactions with increasing scan rate.²¹

The current peak in the CV plot is related to the potential scan rate following a power law: $I_p = a \nu^b$, where I_p is the current peak intensity, a and b are fitting coefficients, and ν is the scan rate.^{5,39} This equation is used to determine the rate-limiting step and kinetic information on the electrochemical reaction. It was found that b has values between 0.5 and 1, where it is ≈ 0.5 for a redox reaction limited by semi-infinite diffusion and ≈ 1 for a capacitive process (which is attributed to the battery and capacitive behavior, respectively).^{40,41} The current peak (I_p) at the different potential scan rates has been shown in Fig. 4d for all the samples. The solid lines in Fig. 4d show the best fitting of this power law equation to the experimental data. The obtained values of b have been presented in Table I. b parameter is 0.91 and 0.56 for the $\text{Fe}_2\text{O}_3/\text{rGO}$ and the $\text{Fe}_3\text{O}_4/\text{rGO}$ binary nanohybrid, respectively. It reveals that the $\text{Fe}_3\text{O}_4/\text{rGO}$ exhibits a battery-type behavior, and redox reactions play a main contribution role in the storage mechanism. In contrast, the $\text{Fe}_2\text{O}_3/\text{rGO}$ exhibits capacitive-type behavior. However, by adding PPy to the $\text{Fe}_3\text{O}_4/\text{rGO}$ binary nanohybrid, the b parameter increases to 0.91 for $\text{Fe}_3\text{O}_4/\text{rGO}/\text{PPy}$. It can be attributed to a decrease in the redox reactions in $\text{Fe}_3\text{O}_4/\text{rGO}/\text{PPy}$ nanocomposite due to π - π interactions between $\text{Fe}_3\text{O}_4/\text{rGO}$ and PPy chains. Thus, $\text{Fe}_3\text{O}_4/\text{rGO}/\text{PPy}$ nanocomposite exhibits capacitance behavior. In contrast, the b parameter for $\text{Fe}_2\text{O}_3/\text{rGO}/\text{PPy}$ decreases to 0.71. It can be attributed to the existence of π -orbitals in PPy chains and increase redox reactions. Therefore, both mechanisms of charge storage play a role in it, and its specific capacitance dramatically increases. The b value of $\text{Fe}_2\text{O}_3/\text{rGO}@/\text{Fe}_3\text{O}_4/\text{rGO} / \text{PPy}$ hybrid nanocomposite is 0.99, which fully exhibits a capacitive behavior. In this hybrid nanocomposite, both the capacitive behavior of $\text{Fe}_2\text{O}_3/\text{rGO}$ and π - π interactions between $\text{Fe}_3\text{O}_4/\text{rGO}$ and PPy significantly decrease redox reactions. It can lead to a decrement in its specific capacitance than the calculated value.

The electrochemical performance of the samples was evaluated by GCD measurements under constant current densities of 1, 2, 3, 5, and 10 A g^{-1} for the first cycle. Figure 5a displays the GCD plots of

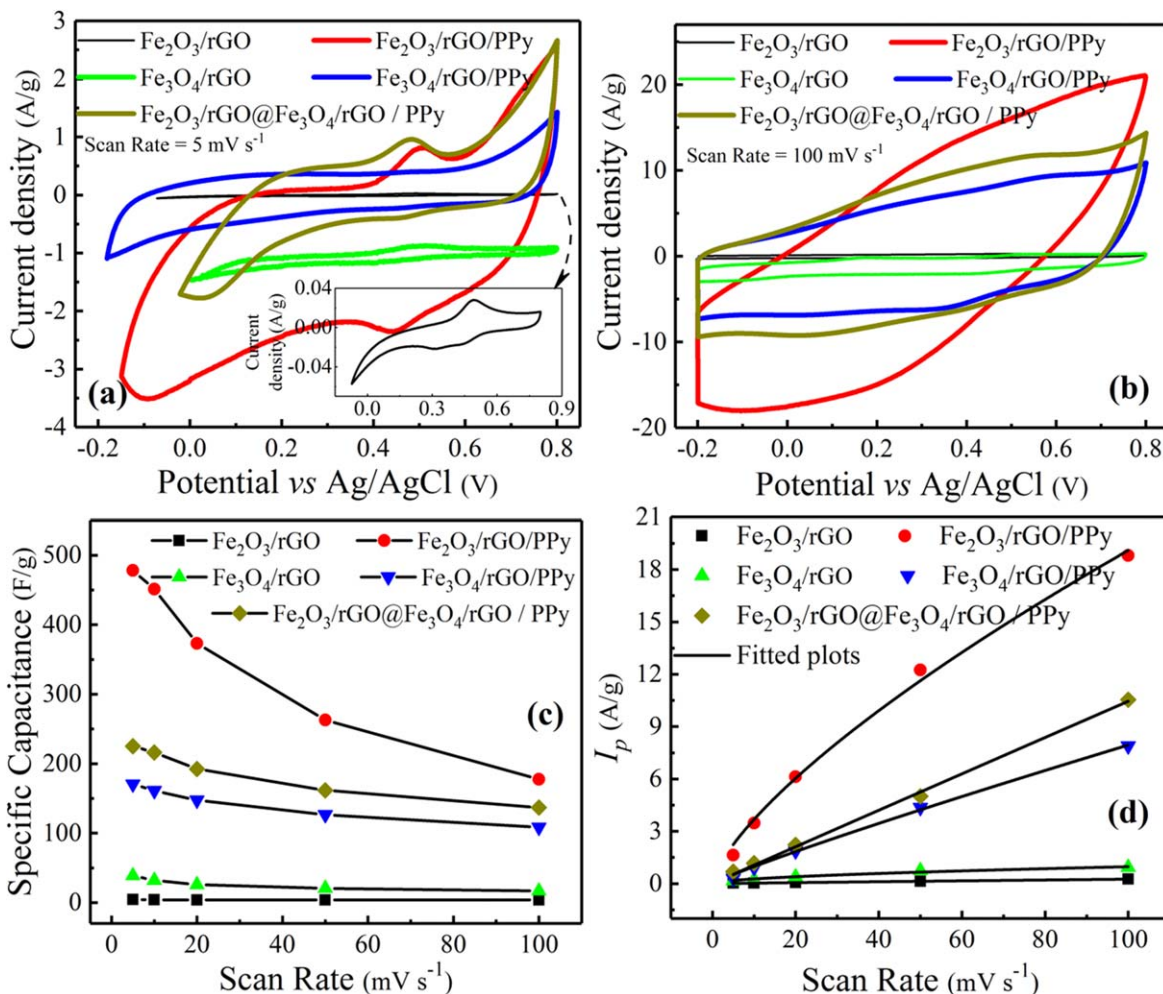


Figure 4. CV plots at a scan rate of (a) 5 and (b) 100 mV s⁻¹; (c) specific capacitance and (d) peak current behavior vs scan rates for all the samples.

Table I. The obtained values of the *b* parameter for all the samples.

	Fe ₂ O ₃ /rGO	Fe ₂ O ₃ /rGO/PPy	Fe ₃ O ₄ /rGO	Fe ₃ O ₄ /rGO/PPy	Fe ₂ O ₃ /rGO@Fe ₃ O ₄ /rGO/PPy
<i>b</i>	0.91 ± 0.031	0.71 ± 0.037	0.56 ± 0.061	0.91 ± 0.035	0.99 ± 0.003

all the samples at a current density of 1 A g⁻¹, representing a deviated triangular shape that signifies the faradaic capacitance and pseudocapacitive behavior. The longer discharge time of ternary nanocomposites indicates a significantly higher specific capacitance. The GCD plots of Fe₂O₃/rGO/PPy nanocomposite have been shown in Fig. 5b at different current densities. The GCD curves of other samples have been shown in SI (Figs. S7–10). The specific capacitance was calculated from the GCD plot using Eq. 2 for the samples, and results are shown in Fig. 5c. The maximum obtained specific capacitance is 626.8 and 158.2 F g⁻¹ for Fe₂O₃/rGO/PPy and Fe₃O₄/rGO/PPy ternary nanocomposite at 1 A g⁻¹, respectively, exhibiting a dramatic increase compared to their binary nanohybrids. The theoretical specific capacitance of iron oxide/rGO/PPy nanocomposite can be calculated by $C_{S_{iron\ oxide/rGO/PPy}} = R_{iron\ oxide/rGO} C_{S_{iron\ oxide/rGO}} + R_{PPy} C_{S_{PPy}}$, where $R_{iron\ oxide/rGO}$ and R_{PPy} are weight percentage of iron oxide/rGO and PPy, respectively, and $C_{S_{iron\ oxide/rGO}}$ and $C_{S_{PPy}}$ are the specific capacitance of iron oxide/rGO nanohybrid and polypyrrole, respectively. It was found⁴² that the specific capacitance of pristine PPy was 36.8 F g⁻¹ at 1 A g⁻¹. For the weight ratio of 10:1 for pyrrole to

iron oxide/rGO, the theoretical specific capacitance of 33.6 and 35.3 F g⁻¹ were obtained for Fe₂O₃/rGO/PPy and Fe₃O₄/rGO/PPy ternary nanocomposite at 1 A g⁻¹, respectively. It reveals that the specific capacitance of Fe₂O₃/rGO/PPy nanocomposite has increased than its components by a factor of 18, that could be assigned to the synergistic effects between nanocomposite components. The specific capacitance of Fe₂O₃/rGO@Fe₃O₄/rGO / PPy hybrid nanocomposite is 201.6 F g⁻¹ at the same current density.

The PPy/Fe₂O₃/rGO ternary composite, as a supercapacitor electrode, was prepared by Moysiewicz et al. using a two-step route via hydrothermal synthesis of the Fe₂O₃/rGO composite followed by polymerization of pyrrole on the Fe₂O₃/rGO surface.¹⁷ The mass ratio of PPy, Fe₂O₃ and rGO in this composite was 50:25:25, respectively. This ternary composite exhibited a specific capacitance of 140 F g⁻¹ at 1 A g⁻¹. But in this work, Fe₂O₃/rGO was prepared by microwave method, in which reduction and exfoliation of GO, and decoration of Fe₂O₃ nanoparticles on GO sheets was well carried out. The adjusted mass ratio of PPy, Fe₂O₃ and rGO in the Fe₂O₃/rGO/PPy nanocomposite was 90:6.65:3.35, respectively. Results shown that the maximum specific capacitance

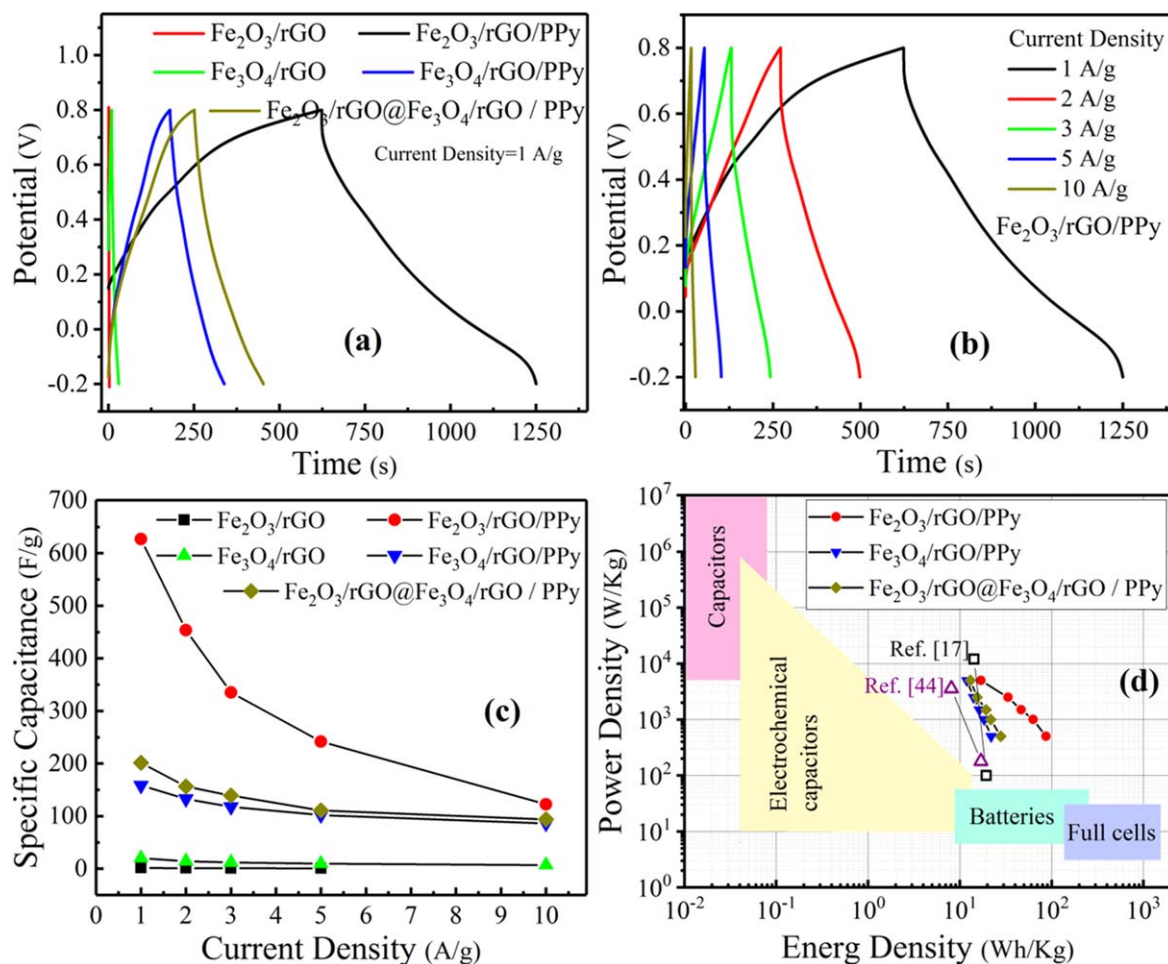


Figure 5. GCD plots (a) for all the samples, and (b) for $\text{Fe}_2\text{O}_3/\text{rGO}/\text{PPy}$ nanocomposite. (c) Specific capacitance as a function of current density for the samples. (d) Ragone plot for ternary and hybrid nanocomposites.

of this ternary nanocomposite was 626.8 F g^{-1} at 1 A g^{-1} , exhibiting an excellent enhancement in comparison of reported work.¹⁷ It can be assigned to proper synthesis method and mass ratio of components. The weight ratio of 10:1 for pyrrole to $\text{Fe}_2\text{O}_3/\text{rGO}$ can lead to improvement of conductivity.

The relationship between the energy density (E) and power density (P), known as the Ragone plot, is an essential factor for the electrode materials. The specific E and P are given by using the equations of $E = C_s^{dis} V^2/2$ and $P = E/t$, where C_s^{dis} is the GCD specific capacitance in F g^{-1} , and V and t are potential window in V, and discharge time in s, respectively. Figure 5d illustrates the Ragone plot for ternary and hybrid nanocomposites. The $\text{Fe}_2\text{O}_3/\text{rGO}/\text{PPy}$ nanocomposite exhibits the highest energy density of 87.05 Wh kg^{-1} with a power density of 500 W kg^{-1} at a current density of 1 A g^{-1} . Such high energy density can be ascribed by the ability of the electrolyte ions to diffuse the porosity of the electrode material and the presence of proper pseudocapacitance behavior due to synergistic effects.⁴³ At the high current density of 10 A g^{-1} , this nanocomposite has attained a high power density of 5000 W kg^{-1} with an energy density of 17.02 Wh kg^{-1} . The decreasing energy density at this high current density, can be due to time deficiency of ions diffusion to the electrode material.⁴³ The maximum energy density of 21.97 and 28 Wh kg^{-1} was obtained for $\text{Fe}_3\text{O}_4/\text{rGO}/\text{PPy}$ nanocomposite and $\text{Fe}_2\text{O}_3/\text{rGO}@/\text{Fe}_3\text{O}_4/\text{rGO}/\text{PPy}$ hybrid nanocomposite along with a power density of 500 W kg^{-1} , respectively. In Fig. 5d, The Ragone plot of these nanocomposites has been compared with similar reported materials (including $\text{PPy}/\text{Fe}_2\text{O}_3/\text{rGO}$ ¹⁷ and $\text{rGO}-\text{Fe}_3\text{O}_4$ ⁴⁴) and other conventional energy storage systems.²⁷ In Table II, the electrochemical performance of

the current work samples has been compared with similar reported electrode materials.

The electrochemical impedance spectra were evaluated to determine the charge kinetic and frequency properties of these electrochemical systems. Nyquist plots can illustrate the frequency response of the electrode/electrolyte system in terms of an imaginary (Z'') and real (Z') part of the impedance. The Nyquist plots have been shown in Fig. 6a for the iron oxides/rGO/PPy ternary and hybrid nanocomposites in the frequency range of 10^{-2} – 10^5 Hz. The solid lines in Fig. 5a are the result of fitting with an equivalent circuit illustrated in the inset of Fig. 6a. The combination of electrolyte resistance, intrinsic resistance of active electrode material, and active-material/collector contact resistance called R_s , is determined from the intercept of the real impedance axis at very high-frequencies.^{43,49} R_{ct} is charge-transfer resistance between electroactive material and electrolyte in the electrochemical process. The equivalent circuit in the inset of Fig. 6a consists of R_{ct} in series with a Warburg impedance (Z_w) and both in parallel with a constant phase element (CPE), which presents a modified Randles circuit cell.⁵⁰ R_L is the limit resistance, and C_F is faradaic capacitance.^{51,52} The obtained values of parameters based upon the best fitting of the equivalent circuit to the experimental data are presented in Table SI (see Supporting Information). The equivalent series resistance (ESR) of the system is evaluated with R_s , R_{ct} , and R_L . The obtained ESR values exhibit $ESR_{\text{Fe}_2\text{O}_3/\text{ternary}} < ESR_{\text{Hybrid}} < ESR_{\text{Fe}_3\text{O}_4/\text{ternary}}$, revealing the conductivity effect on improving specific capacitance.

The frequency dependence of the electrode behavior, such as complex resistance $Z(\omega)$, phase angle $\Phi(\omega)$, and capacitance $C(\omega)$, can be used to study capacitive and resistive behavior at different

Table II. Comparison of electrochemical performance of the current work samples with similar reported electrode materials.

Sample	Synthesis Method	Electrolyte	Specific capacitance	Power density	Energy density	Working voltage (V)	References.
α -Fe ₂ O ₃ /G	Hydrothermal	2 M KOH	315 F g ⁻¹ at 2 A g ⁻¹	—	—	-0.4-0.2	45
rGO/Fe ₂ O ₃	One-step chemical	0.5 M H ₂ SO ₄	50 F g ⁻¹ at 0.1 V s ⁻¹ 138.5 F/g at 0.3 A g ⁻¹	—	—	-0.2-1	30
PPy/rGO/Fe ₂ O ₃	Electrodeposition	1.0 M KCl	125.7 F g ⁻¹ at 0.5 A g ⁻¹	—	—	-0.5-0.5	46
PPy/Fe ₂ O ₃ /rGO	Hydrothermal/oxidative polymerization	1 M Na ₂ SO ₄	140 F g ⁻¹ at 1 A g ⁻¹	12 kW kg ⁻¹ (at energy density of 14.3 Wh kg ⁻¹)	19.5 Wh kg ⁻¹ (at power density of 0.1 kW kg ⁻¹)	-1-0	17
Fe ₃ O ₄ /rGO	One-pot microwave	2 M KOH	455 F g ⁻¹ at 8 mV s ⁻¹	—	—	-1-0.4	47
rGO-Fe ₃ O ₄	Electrophoretic deposition	0.5 M Na ₂ SO ₄ (containing Triton X-100)	236 F g ⁻¹ at 1 A g ⁻¹	3.6 kW kg ⁻¹ (at energy density of 8.1 Wh kg ⁻¹)	17 Wh kg ⁻¹ (at power density of 180 W kg ⁻¹)	0-0.8	44
rGO/Fe ₃ O ₄ /PAni	Hydrothermal/in situ hydrothermal polymerization	1 M H ₂ SO ₄	486.5 F/g at 1 A g ⁻¹	—	—	0-0.8	48
Fe ₂ O ₃ /rGO/PPy	Chemical-microwave/in situ polymerization	1 M H ₂ SO ₄	626.8 F g ⁻¹ at 1 A g ⁻¹	5 kW kg ⁻¹ (at energy density of 17.02 Wh kg ⁻¹)	87.05 Wh kg ⁻¹ (at power density of 500 W kg ⁻¹)	-0.2-0.8	This work
Fe ₃ O ₄ /rGO/PPy	Chemical-microwave/in situ polymerization	1 M H ₂ SO ₄	158.2 F g ⁻¹ at 1 A g ⁻¹	5 kW kg ⁻¹ (at energy density of 11.94 Wh kg ⁻¹)	21.97 Wh kg ⁻¹ (at power density of 500 W kg ⁻¹)	-0.2-0.8	This work
Fe ₂ O ₃ /rGO@Fe ₃ O ₄ /rGO/PPy	Chemical-microwave/in situ polymerization	1 M H ₂ SO ₄	201.6 F/g at 1 A g ⁻¹	5 kW kg ⁻¹ (at energy density of 13.05 Wh kg ⁻¹)	28 Wh kg ⁻¹ (at power density of 500 W kg ⁻¹)	-0.2-0.8	This work

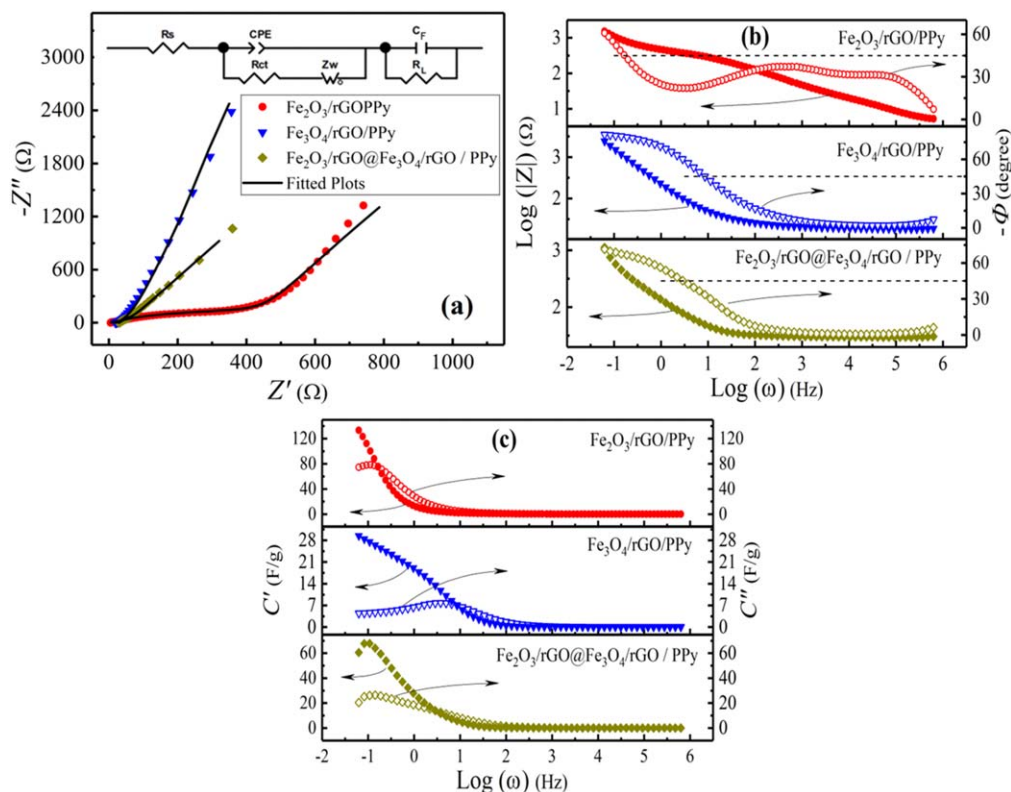


Figure 6. (a) The Nyquist plot for iron oxides/rGO/PPy ternary and hybrid nanocomposites and their fitted lines. The electrical equivalent circuit has been represented in the inset. (b) The magnitude of complex resistance and the phase angle, and (c) the real (C') and imaginary (C'') parts of complex specific capacitance vs $\log(\omega)$ for ternary and hybrid nanocomposites.

regions of frequency (ω is the angular frequency). The magnitude of complex resistance ($\log |Z|$) and the phase angle have been shown in Fig. 6b as a function of frequency ($\log \omega$) for the iron oxides/rGO/PPy ternary and hybrid nanocomposites. The low-frequency region can be considered the near -1 slope in $\log |Z|$ plot. This region corresponds to the linear part of the Nyquist plot, and the electrode exhibits a typical capacitive behavior.⁵³ The low-frequency region was below the frequency of 0.03, 0.80, and 0.12 Hz for the Fe_2O_3 ternary, the Fe_3O_4 ternary, and the hybrid nanocomposite, respectively. It can reveal that although the specific capacitance of $\text{Fe}_2\text{O}_3/\text{rGO}/\text{PPy}$ is larger than the $\text{Fe}_3\text{O}_4/\text{rGO}/\text{PPy}$ nanocomposite, the $\text{Fe}_2\text{O}_3/\text{rGO}/\text{PPy}$ exhibits capacitive behavior in a smaller frequency range. The resistive behavior appears at a higher frequency for them. In addition, the corresponding frequency to -45° phase angle shown in Fig. 6b, can be related to the capacitor response frequency.⁵³ This frequency was 0.026, 1.37, and 0.46 Hz for the Fe_2O_3 ternary, the Fe_3O_4 ternary, and hybrid nanocomposite, respectively. These values signify that the response time of the $\text{Fe}_3\text{O}_4/\text{rGO}/\text{PPy}$ electrode is much shorter than the $\text{Fe}_2\text{O}_3/\text{rGO}/\text{PPy}$ electrode. It can be attributed to a double-layer charge storage mechanism in the $\text{Fe}_3\text{O}_4/\text{rGO}/\text{PPy}$ and pseudocapacitive behavior in the $\text{Fe}_2\text{O}_3/\text{rGO}/\text{PPy}$ nanocomposite. Also, this deduction is supported by obtained results from the current peak (I_p) in the CV plot, as illustrated in Table I.

The real (C') and imaginary (C'') parts of complex specific capacitance can be inferred from the complex impedance from the following equations⁵⁴:

$$C'(\omega) = \frac{-Z''(\omega)}{m\omega |Z(\omega)|^2} \quad [3]$$

$$C''(\omega) = \frac{Z'(\omega)}{m\omega |Z(\omega)|^2} \quad [4]$$

C' and C'' correspond to the charges in available stored energy and energy dissipation process as a function of frequency, respectively. C' and C'' have been illustrated in Fig. 6c as a function of frequency for the iron oxides/rGO/PPy ternary and the hybrid nanocomposite. The characteristic frequency of f_0 can divide the electrode behavior predominantly into capacitive behavior at frequencies below f_0 , and resistive behavior at the frequencies higher than f_0 . The f_0 can be determined from the peak frequency of C'' .⁵⁵

The relaxation time constant, τ_0 ($=\frac{1}{f_0}$), which is a minimum time required to discharge all of the stored energy from electrode material, can be deduced from the complex capacitance plots. The f_0 values of 0.018, 0.602, and 0.023 Hz were obtained for the Fe_2O_3 ternary, the Fe_3O_4 ternary, and the hybrid nanocomposite, respectively. It means that these nanocomposites exhibit an ideal capacitive behavior only at very low frequency.

Conclusions

Iron oxides/rGO (Fe_2O_3 and Fe_3O_4) binary nanohybrid, iron oxides/rGO/PPy ternary nanocomposite, and $\text{Fe}_2\text{O}_3/\text{rGO}@/\text{Fe}_3\text{O}_4/\text{rGO}/\text{PPy}$ hybrid nanocomposite were synthesized as electrode materials of a supercapacitor. The proper formation of these nanocomposites was confirmed by TEM, XRD, XPS, FTIR, and Raman spectroscopy. At a current density of 1 A g^{-1} , a maximum specific capacitance of 626.8, 158.2, and 201.6 F g^{-1} was obtained for the Fe_2O_3 ternary, the Fe_3O_4 ternary, and the hybrid nanocomposite, respectively. The $\text{Fe}_2\text{O}_3/\text{rGO}/\text{PPy}$ nanocomposite exhibited the highest energy density of 87.05 Wh kg^{-1} with a corresponding power density of 500 W kg^{-1} . This high specific capacitance and energy density can be assigned to the presence of

both EDLC and pseudocapacitance mechanisms in its charge storage. The impedance spectroscopy and frequency dependence study exhibited an ideal capacitive behavior only at a very low frequency for these ternary nanocomposites.

Acknowledgments

The authors acknowledge funding from the National Natural Science Foundation of China (Grant no. 51761135113) and the Ferdowsi University of Mashhad (Grant no. 3/42918).

ORCID

R. Ghanbari  <https://orcid.org/0000-0002-4557-4943>

S. R. Ghorbani  <https://orcid.org/0000-0001-6315-7812>

References

1. Y. Huang, H. Li, Z. Wang, M. Zhu, Z. Pei, Q. Xue, Y. Huang, and C. Zhi, *Nano Energy*, **22**, 422 (2016).
2. W. Zuo, R. Li, C. Zhou, Y. Li, J. Xia, and J. Liu, *Adv. Sci.*, **4**, 1600539 (2017).
3. D. P. Dubal, O. Ayyad, V. Ruiz, and P. Gomez-Romero, *Chem. Soc. Rev.*, **44**, 1777 (2015).
4. M. Winter and R. J. Brodd, *Chem. Rev.*, **104**, 4245 (2004).
5. P. Simon, Y. Gogotsi, and B. Dunn, *Science*, **343**, 1210 (2014).
6. F. Yao, D. T. Pham, and Y. H. Lee, *ChemSusChem*, **8**, 2284 (2015).
7. W. K. Chee, H. N. Lim, I. Harrison, K. F. Chong, Z. Zainal, C. H. Ng, and N. M. Huang, *Electrochim. Acta*, **157**, 88 (2015).
8. L. Hao, X. Li, and L. Zhi, *Adv. Mater.*, **25**, 3899 (2013).
9. J. Yan, T. Wei, W. Qiao, B. Shao, Q. Zhao, L. Zhang, and Z. Fan, *Electrochim. Acta*, **55**, 6973 (2010).
10. L. Li, Z. Guo, A. Du, and H. Liu, *J. Mater. Chem.*, **22**, 3600 (2012).
11. X. Wu, L. Meng, Q. Wang, W. Zhang, and Y. Wang, *Mater. Chem. Phys.*, **206**, 259 (2018).
12. J. Zhang and X. S. Zhao, *J. Phys. Chem. C*, **116**, 5420 (2012).
13. H. Wang, Q. Hao, X. Yang, L. Lu, and X. Wang, *Nanoscale*, **2**, 2164 (2010).
14. Y. Zhu, S. Murali, W. Cai, X. Li, J. W. Suk, J. R. Potts, and R. S. Ruoff, *Adv. Mater.*, **22**, 3906 (2010).
15. G. Han, Y. Liu, E. Kan, J. Tang, L. Zhang, H. Wang, and W. Tang, *RSC Adv.*, **4**, 9898 (2014).
16. M. Zhi, C. Xiang, J. Li, M. Li, and N. Wu, *Nanoscale*, **5**, 72 (2013).
17. A. Moysiewicz, A. Sliwak, E. Miniach, and G. Gryglewicz, *Compos. B. Eng.*, **109**, 23 (2017).
18. Y. S. Lim, Y. P. Tan, H. N. Lim, N. M. Huang, W. T. Tan, M. A. Yarmo, and C.-Y. Yin, *Ceram. Int.*, **40**, 3855 (2014).
19. A. K. Das, S. K. Karan, and B. B. Khatua, *Electrochim. Acta*, **180**, 1 (2015).
20. S. Ishaq, M. Moussa, F. Kanwal, M. Ehsan, M. Saleem, T. N. Van, and D. Losic, *Sci. Rep.*, **9**, 5974 (2019).
21. B. S. Singu and K. R. Yoon, *Electrochim. Acta*, **268**, 304 (2018).
22. W. Wang, Q. Hao, W. Lei, X. Xia, and X. Wang, *RSC Adv.*, **2**, 10268 (2012).
23. X. Zhu, Y. Zhu, S. Murali, M. D. Stoller, and R. S. Ruoff, *ACS Nano*, **5**, 3333 (2011).
24. S. Vadahanambi, J.-H. Jung, and I.-K. Oh, *Carbon*, **49**, 4449 (2011).
25. W. S. Hummers and R. E. Offeman, *J. Am. Chem. Soc.*, **80**, 1339 (1958).
26. Y. Liu, H. Wang, J. Zhou, L. Bian, E. Zhu, J. Hai, J. Tang, and W. Tang, *Electrochim. Acta*, **112**, 44 (2013).
27. D. Ghosh, S. Giri, S. Dhibar, and C. K. Das, *Electrochim. Acta*, **147**, 557 (2014).
28. X. Wang, Y. Liu, H. Arandiyani, H. Yang, L. Bai, J. Muftaba, Q. Wang, S. Liu, and H. Sun, *Appl. Surf. Sci.*, **389**, 240 (2016).
29. C. Fu, G. Zhao, H. Zhang, and S. Li, *Int. J. Electrochem. Sci.*, **9**, 946 (2014).
30. R. Bhujel, S. Rai, U. Deka, and B. P. Swain, *J. Alloys Compd.*, **792**, 250 (2019).
31. J. Wang, X. Wang, Y. Song, J. Wang, C. Zhang, C. Chang, J. Yan, L. Qiu, M. Wu, and Z. Guo, *Chem. Sci.*, **4**, 2605 (2013).
32. H. Di, Z. Yu, Y. Ma, F. Li, L. Lv, Y. Pan, Y. Lin, Y. Liu, and Y. He, *J. Taiwan Inst. Chem. Eng.*, **64**, 244 (2016).
33. S. B. Kayode and A. A. Aziz, *Adv. Mater. Res.*, **1024**, 300 (2015).
34. S. Stankovich, D. A. Dikin, R. D. Piner, K. A. Kohlhaas, A. Kleinhammes, Y. Jia, Y. Wu, S. T. Nguyen, and R. S. Ruoff, *Carbon*, **45**, 1558 (2007).
35. C. Xu, J. Sun, and L. Gao, *J. Mater. Chem.*, **21**, 11253 (2011).
36. A. Schaarschmidt, A. A. Farah, A. Aby, and A. S. Helmy, *J. Phys. Chem. B*, **113**, 9352 (2009).
37. S. Bhuvaneshwari, P. M. Pratheeksha, S. Anandan, D. Rangappa, R. Gopalan, and T. N. Rao, *Phys. Chem. Chem. Phys.*, **16**, 5284 (2014).
38. Y. Zhao, X. Song, Q. Song, and Z. Yin, *Cryst. Eng. Comm.*, **14**, 6710 (2012).
39. H. Lindstrom, S. Sodergren, A. Solbrand, H. Rensmo, J. Hjelm, A. Hagfeldt, and S.-E. Lindquist, *J. Phys. Chem. B*, **101**, 7710 (1997).
40. V. Augustyn, J. Come, M. A. Lowe, J. W. Kim, P.-L. Taberna, S. H. Tolbert, H. D. Abruna, P. Simon, and B. Dunn, *Nat. Mater.*, **12**, 518 (2013).
41. J. Come, P. L. Taberna, S. Hamelet, C. Masquelier, and P. Simon, *J. Electrochem. Soc.*, **158**, A1090 (2011).
42. R. Ghanbari, M. Entezar Shabestari, E. Naderi Kalali, Y. Hu, and S. R. Ghorbani, *Ionics*, **27**, 1279 (2021).
43. M. D. Stoller, S. Park, Y. Zhu, J. An, and R. S. Ruoff, *Nano Lett.*, **8**, 3498 (2008).
44. S. Ghasemi and F. Ahmadi, *J. Power Sources*, **289**, 129 (2015).
45. M. Jayashree, M. Parthibavarman, and S. Prabhakaran, *Ionics*, **25**, 3309 (2019).
46. Y. C. Eue, H. N. Lim, Y. S. Lim, S. A. Zakarya, and N. M. Huang, *J. Nanomater.*, **2013**, 3653890 (2013).
47. R. Kumar, R. K. Singh, A. R. Vaz, R. Savu, and S. A. Moshkalev, *ACS Appl. Mater. Interfaces*, **9**, 8880 (2017).
48. M. M. Mezgebe, Z. Yan, G. Wei, S. Gong, F. Zhang, S. Guang, and H. Xu, *Mater. Today Energy*, **5**, 164 (2017).
49. J. P. Mensing, A. Wisitsoraat, D. Phokharatkul, T. Lomas, and A. Tuantranont, *Compos. B. Eng.*, **77**, 93 (2015).
50. X.-Z. Yuan, C. Song, H. Wang, and J. Zhang, *Electrochemical Impedance Spectroscopy in PEM Fuel Cells: Fundamentals and Applications* (Springer, Berlin) (2010).
51. A. Di Fabio, A. Giorgi, M. Mastragostino, and F. Soavi, *J. Electrochem. Soc.*, **148**, A845 (2001).
52. T. Purkait, G. Singh, D. Kumar, M. Singh, and R. S. Dey, *Sci. Rep.*, **8**, 640 (2018).
53. G. Zhao, N. Zhang, and K. Sun, *Mater. Res. Bull.*, **48**, 1328 (2013).
54. G. A. M. Ali, M. M. Yusoff, E. R. Shaaban, and K. F. Chong, *Ceram. Int.*, **43**, 8440 (2017).
55. R. A. Aziz, I. I. Misnon, K. F. Chong, M. M. Yusoff, and R. Jose, *Electrochim. Acta*, **113**, 141 (2013).